**Article:**
Nag, Aniruddha (2026) Data-Efficient Mapping of Copolymerization Curves and Reactivity Ratios via Gradient Flow Polymerization, Inline ATR-FTIR, and Lasso Regression. ACS Omega. 45574–45587. ISSN: 2470-1343

https://doi.org/10.1021/acsomega.6c06915

ACS OMEGA

Open Access



http://pubs.acs.org/journal/acsodf

Article

# Data-Efficient Mapping of Copolymerization Curves and Reactivity Ratios via Gradient Flow Polymerization, Inline ATR-FTIR, and Lasso Regression

Araki Wakiuchi, Aniruddha Nag, Swarit Jasial, Masashi Nakayama, Shogo Takasuka, Shigehito Asano, Ryo Hashizume, Miho Hatanaka, Yu-ya Ohnishi, Takamitsu Matsubara, Tsuyoshi Ando, Tetsunori Sugawara, Mikiya Fujii, Tomoyuki Miyao,* and Hiroharu Ajiro*

Cite This: *ACS Omega* 2026, 11, 45574−45587

Read Online

ACCESS | Metrics & More | Article Recommendations | Supporting Information

**ABSTRACT:** Copolymerization curves and reactivity-ratio estimates are traditionally derived from sparse offline data collected across many separate experiments. Here, we propose a data-efficient workflow for apparent finite-conversion reactivity-ratio estimation that combines gradient continuous-flow free-radical copolymerization, inline ATR-FTIR spectroscopy, and sparse linear regression to reconstruct dense concentration and composition trajectories from minimal offline quantitation. Using styrene/methyl methacrylate as a benchmark system, we performed a time-programmed zigzag sweep of the styrene/MMA feed ratio at constant total flow and acquired more than 700 inline ATR-FTIR spectra in a single ∼4 h run at each of 70, 80, and 90 °C. Only ten offline UHPLC anchor points per run were used to calibrate Lasso models for monomer concentration prediction, enabling high-density reconstruction of the reference monomer composition $f_1(t)$, total conversion $X_{tot}(t)$, and cumulative consumption-based copolymer-composition proxy $F_{1,cum}(t)$. The reconstructed finite-conversion trajectories were analyzed using a Skeist-type finite-conversion terminal-model formulation, in which the Mayo−Lewis equation was used as the instantaneous composition relation. The maximum $X_{tot}$ values spanned 0.36−0.62, and the full-data IR-assisted estimates spanned $r_1$ = 0.33−0.48 and $r_2$ = 0.39−0.44, remaining within the broad range of benchmark literature values for this system. Residual-based Monte Carlo sampling showed that pointwise concentration-prediction uncertainty led to compact $r_1$−$r_2$ ensembles, whereas block-removal and UHPLC-only subset analyses revealed sensitivity to sparse-anchor selection, most notably at 70 °C. Because the workflow uses finite-conversion trajectory data, aligned reference/reacting concentration differences, and this $F_{1,cum}$ proxy, the reported values are interpreted as apparent finite-conversion estimates under the present flow and analysis workflow. This approach provides a practical route to dense, uncertainty-aware copolymerization-trajectory mapping from minimal offline measurements and enables unified comparison of apparent finite-conversion reactivity-ratio estimates across temperatures.

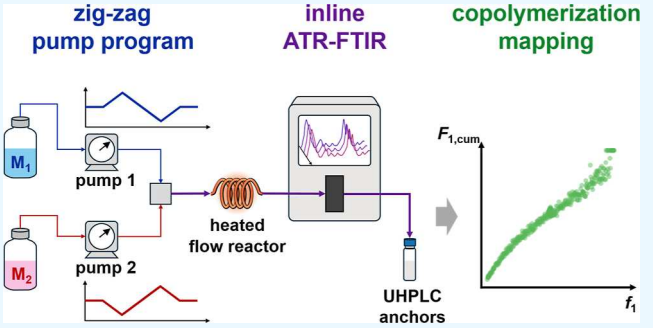


## 1. INTRODUCTION

The instantaneous relationship between copolymer composition and monomer composition is commonly described by the Mayo−Lewis equation under the terminal model, which permits a description using the reactivity ratios $r_1$ and $r_2$.[1−3] The theory was proposed by Frank R. Mayo and Frederick M. Lewis in their seminal 1944 paper.[4] The Mayo−Lewis equation has been widely accepted as a foundation for copolymer design, and its influence remains strong after more than 80 years of investigation, with recent comprehensive reviews including numerical estimation techniques.[5] For finite-conversion experiments, however, the residual monomer composition changes as polymerization proceeds, and experimentally measured or reconstructed copolymer compositions often correspond to cumulative compositions over a finite conversion interval rather than strictly differential instantaneous compositions. The Skeist formulation provides a finite-conversion framework for calculating cumulative copolymer compositions by integrating the instantaneous terminal-model composition relation over the evolving monomer mixture.[6]

For reactivity ratio estimation, linearization methods such as the Fineman−Ross (FR)[7] and Kelen−Tüdős (KT)[8] methods

Received: June 14, 2026
Revised: July 12, 2026
Accepted: July 14, 2026
Published: July 20, 2026







https://doi.org/10.1021/acsomega.6c06915
*ACS Omega* 2026, 11, 45574−45587

have long been used. However, these methods have been criticized for bias and distorted error structures, and the handling of confidence intervals requires caution.[9] In contrast, nonlinear least-squares (NLLS) and error-in-variables (EVM) methods provide coherent treatments of nonlinearity and measurement errors in all variables, and are generally recommended approaches.[9,10] NLLS was applied to copolymerization problems by Behnken and by Tidwell and Mortimer,[11,12] and since then, visualization of the objective function (sum of squares) contours, or sum-of-squares surfaces (SSS), has become common practice for intuitively assessing $r_1-r_2$ correlation and confidence regions.[3,9,10] Recently, IUPAC proposed recommended experimental and reporting procedures for reactivity ratio determination, emphasizing paired measurements of conversion and copolymer composition at multiple initial monomer ratios, typically including at least three initial feed compositions, and encouraging the combined use of low- and higher-conversion data where appropriate.[3] In conventional batch implementation, the experimental burden arises from preparing and analyzing multiple independent feed-composition/conversion points. The present continuous-flow workflow is aligned with this principle, while automatically varying the comonomer feed ratio within a single run and using Skeist-type finite-conversion analysis to account for composition drift.

Copolymerization of styrene (St) and methyl methacrylate (MMA) is a classic system with a rich research history; Mayo and Lewis reported its copolymerization data in their original article.[4] Reported reactivity ratios (r values) for this system depend on temperature, solvent, and mechanistic extensions (e.g., the penultimate or "implicit penultimate" models).[13,14] For example, classical reports at 90 °C give $r_{St} \approx 0.55$ and $r_{MMA} \approx 0.58$,[15] whereas a recent study using PLP (pulsed-laser polymerization)/MALDI-TOF-MS analyses under a terminal-implicit penultimate model reported $r_{St} \approx 0.52$ and $r_{MMA} \approx 0.42$.[2] More recently, St/MMA copolymerization in benzene-$d_6$ at 60 °C was used as a model system for in situ $^1$H NMR-based reactivity-ratio determination, providing another method-specific benchmark for this system.[16] Solvent effects have long been recognized in St/MMA radical copolymerization.[17] Numerous studies have also examined system dependencies, including nonconventional media such as ionic liquids.[18] Thus, deriving r values under standardized conditions is important.

Traditionally, composition-curve data used to derive reactivity ratios are obtained from many batch experiments at discrete feed compositions. Such data sets are often sparse and can also be affected by run-to-run variability in temperature and conversion. By contrast, continuous-flow reactors offer efficient heat and mass transfer and controllable residence times, enabling dynamic sweeping of feed composition within a single run and rapid sampling across composition space.[19] Indeed, continuous sampling in flow polymerization has demonstrated rapid, multipoint monitoring of reaction progress.[20] One approach determines reactivity ratios by collecting nine low-conversion samples with systematically varied feed compositions within 1 h and fitting the terminal model by NLLS. This approach reported $r_1$ and $r_2$ values consistent with previous studies.[21] Methods for flow polymerization have improved, and they can be applied not only to living radical polymerization[19] but also to free-radical polymerization[22] and gradient copolymerization.[23] Examples include continuous-flow ATRP of MMA[24] and overcoming oxygen sensitivity in RAFT polymerization.[25] We have previously investigated free-radical copolymerization under various conditions using flow reactors.[26−29]

In this context, dense inline data are attractive because they can provide detailed concentration and composition trajectories within a single run. At the same time, when such trajectories are reconstructed from a small number of offline anchor points, the resulting reactivity-ratio estimates still require careful interpretation. A well-studied benchmark system is therefore useful for evaluating how far this type of workflow can support dense copolymerization mapping and reactivity-ratio estimation in practice.

Moreover, continuous-flow operation is highly compatible with online instrumentation, allowing inline/online monitoring of reaction progress during flow.[20,30,31] Studies using inline/online measurements in continuous-flow systems to screen Claisen reaction conditions have been reported.[32] Among online spectroscopies, ATR-FTIR is widely used to monitor conversion and concentration in radical polymerizations because it provides functional-group-specific signals and enables in situ and continuous measurements via flow cells or probes.[30,33] Detailed IR spectral analyses of polyacrylates, including PMMA and polystyrene/PMMA copolymers, have also been reported.[34] In the St/MMA system, MMA's C═O (∼1720 cm$^{-1}$) and C−O (∼1150−1250 cm$^{-1}$) bands and the aromatic bands of St (∼1600 cm$^{-1}$, 770−690 cm$^{-1}$) are useful. We have previously shown the effectiveness of FTIR analysis for estimating comonomer concentration in copolymerization solutions including St/MMA.[35,36] In flow IR, metrological considerations such as sensor placement, flow direction, and flow-cell configuration are important because they can affect response time, signal stability, and data quality.[31]

Chemometric multivariate calibration, most commonly partial least-squares (PLS), is widely used to map spectra to concentrations. As a complementary linear approach, L1-regularized regression (Lasso)[37] promotes sparsity and interpretability by automatically selecting informative wavenumber regions and driving many coefficients to zero, which is well suited to the high-dimensional, highly collinear features typical of IR spectra. Regularization can be tuned by cross-validation, and widely used toolkits provide implementations such as scikit-learn's LassoCV.[38]

Here, we propose a data-efficient workflow to estimate apparent reactivity ratios in gradient-flow free-radical copolymerization using inline ATR-FTIR and sparse offline UHPLC anchoring. The workflow reconstructs dense concentration trajectories from a small number of offline measurements and uses them to generate high-density copolymerization trajectories for reactivity-ratio estimation. The workflow further incorporates Skeist-type finite-conversion terminal-model fitting, residual-based uncertainty propagation via Monte Carlo simulation, and sensitivity analyses based on block removal and sparse-data subset selection. The resulting values are interpreted as apparent finite-conversion reactivity-ratio estimates under the present flow and analysis workflow.

## 2. EXPERIMENTAL SECTION

### 2.1. Workflow Overview

The overall experimental and analytical workflow used in this study is summarized in Figure 1. Styrene (St) and methyl methacrylate (MMA) were copolymerized in a continuous-flow reactor under a zigzag feed-composition program at a fixed total flow rate. A run at 25 °C was recorded as an unreacted reference, and reacting runs were then carried out at 70, 80, and 90 °C. During each run, ATR-FTIR





https://doi.org/10.1021/acsomega.6c06915
ACS Omega 2026, 11, 45574−45587

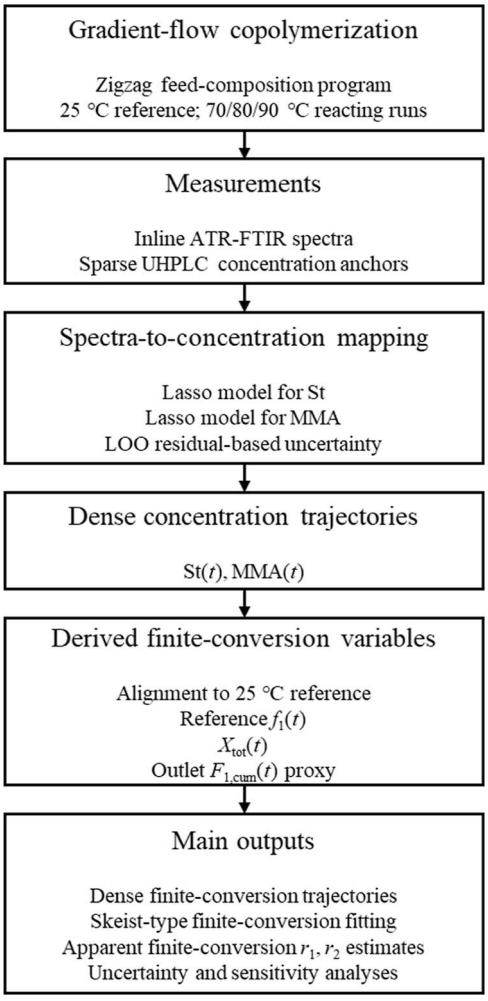


**Figure 1.** Experimental and analytical workflow used in this study. Styrene/MMA copolymerization was carried out in a continuous-flow reactor under a zigzag feed-composition program at a fixed total flow rate. A 25 °C run served as an unreacted reference, and reacting runs were recorded at 70, 80, and 90 °C. Dense inline ATR-FTIR spectra and sparse UHPLC concentration anchors were combined through Lasso-based spectra-to-concentration mapping to reconstruct dense monomer concentration trajectories. Uncertainty in concentration prediction was estimated from interior-anchor leave-one-out residuals and propagated to derived variables and Monte Carlo ensembles. After alignment to the reference trajectory, the reference monomer composition $f_1(t)$, total conversion $X_{tot}(t)$, and outlet composition proxy $F_{1,cum}(t)$ were calculated to generate dense finite-conversion copolymerization trajectories. These trajectories were analyzed using a Skeist-type finite-conversion terminal-model formulation to obtain apparent finite-conversion reactivity-ratio estimates.

spectra were collected inline at high temporal density, while a limited number of outlet samples were analyzed by UHPLC and used as concentration anchors. The paired ATR-FTIR and UHPLC data were used to build sparse Lasso models for St and MMA concentration prediction. Prediction uncertainty was estimated from interior-anchor leave-one-out residuals. The trained models were then applied to the full spectral series to reconstruct dense monomer concentration trajectories. After temporal alignment to the 25 °C reference, the reconstructed concentrations were used to calculate the reference monomer composition $f_1(t)$, the total conversion $X_{tot}(t)$, and the consumption-based outlet composition proxy $F_{1,cum}(t)$. These variables define dense finite-conversion copolymerization trajectories for each run. Apparent reactivity ratios were then obtained using a Skeist-type finite-conversion terminal-model formulation, in which the Mayo−Lewis equation was used as the instantaneous composition relation. The same residual-based uncertainty estimates were propagated by Monte Carlo simulation to the trajectory- and reactivity-ratio-level outputs.

In addition to the core workflow shown in Figure 1, this study includes separate analyses to examine the stability of the results with respect to data selection. These analyses evaluate sensitivity to anchor removal and to sparse-data subset choice. The experimental setup and measurements are described in Sections 2.6, the core data-analysis workflow in Section 2.7, and the sensitivity and robustness analyses in Section 2.8.

## 2.2. Apparatus and Control

Two plunger pumps delivered solutions of styrene with initiator and methyl methacrylate with initiator (reagent bottles kept on ice throughout). The two streams merged and mixed in a micromixer; the downstream tubing served as the reactor segment maintained in a thermostated water bath. Inline IR was performed with a DS micro flow cell (DiComp (diamond) ATR attachment) mounted on a ReactIR 15 instrument (Mettler Toledo), measuring the flowing stream directly. The reagent structures and polymerization scheme and photographs/schematics of the setup and plumbing are shown in Figure 2.

The continuous-flow copolymerization setup consisted of: plunger pumps (DFC, FC-F-PP-410S), four-port screw caps (Duran Wheaton Kimble, 017270 3A), PFA tubing (tetrafluoroethylene−perfluoroalkoxyvinyl ether copolymer; 10 m (2 mm i.d., 3 mm o.d.)) placed in a programmable thermostatic bath (EYELA, NTB-221), a micromixer (YMC, KC-M-Y-GL) with housing (YMC, YMC-P-0030-02), a USB-serial cable (Buffalo, BSUSRC0610BS), an RS-232C cross cable (Sanwa Supply, KRS 403XF1K2), and an RS-485C cable (DFC, PF505 01 500L). Ultra high performance liquid chromatography (UHPLC; Nexera XS, Shimadzu: DGU-403, LC-40D XS, SIL-40C XS, CBM-40, RID-20A, SPD-M40, CTO-40C) equipped with a separation column (GL Science, ODS-3, 2 $\mu$m, 3.0 × 50 mm) was used to quantify residual monomer concentrations (styrene and MMA) using DMF as an internal standard; copolymer composition was inferred from monomer consumption relative to the unreacted reference as described in Section 2.7.3. Size-exclusion chromatography (SEC; same platform) equipped with a SEC column (TSKgel SuperHM-M, 6.0 mm I.D. × 15 cm, 3 $\mu$m) was used to determine number-average ($M_n$) and weight-average ($M_w$) molar masses. Pumps were controlled via serial communication from a Windows laptop running Python 3.10 with PySerial (v3.5). The thermostatic bath was monitored on the same laptop using the vendor software. A dedicated Windows PC running the vendor software was used to control a ReactIR 15.

## 2.3. Reagents and Feed Composition

Two monomers were used: St (FUJIFILM Wako Pure Chemical Co., special grade) and MMA (TCI, stabilized with 6-*tert*-butyl-2,4-xylenol), each dissolved in propylene glycol monomethyl ether (PGME) to 20 wt %. Initiator 2,2′-azobis(2,4-dimethylvaleronitrile) (ADVN; FUJIFILM Wako Pure Chemical Co., first grade) was added at 2 mol % relative to monomer in both feed solutions, so that the overall initiator-to-total-monomer ratio was nominally kept constant during the composition sweep. An example feed is as follows.

- Solution A: St 47.48 g, ADVN 2.265 g, PGME 189.9 g.
- Solution B: MMA 47.48 g, ADVN 2.356 g, PGME 189.9 g.

Densities of the mixed solutions were measured using a 50 mL volumetric flask and an electronic balance readable to four decimal places; the values were 0.912 g mL$^{-1}$ and 0.920 g mL$^{-1}$, respectively.

## 2.4. Flow-Rate Program and Temperature Conditions

The total flow rate was fixed at 1.5 mL min$^{-1}$; initially, both pumps were stabilized at 0.75 mL min$^{-1}$. Thereafter, every 30 s, pump A was increased by +0.01 mL min$^{-1}$ and pump B decreased by −0.01 mL min$^{-1}$ to continuously sweep the feed ratio. Upon pump A reaching 1.5 mL min$^{-1}$, the direction was reversed; upon reaching 0 mL min$^{-1}$, it was reversed again, and the run was stopped once both returned to




https://doi.org/10.1021/acsomega.6c06915
ACS Omega 2026, 11, 45574−45587

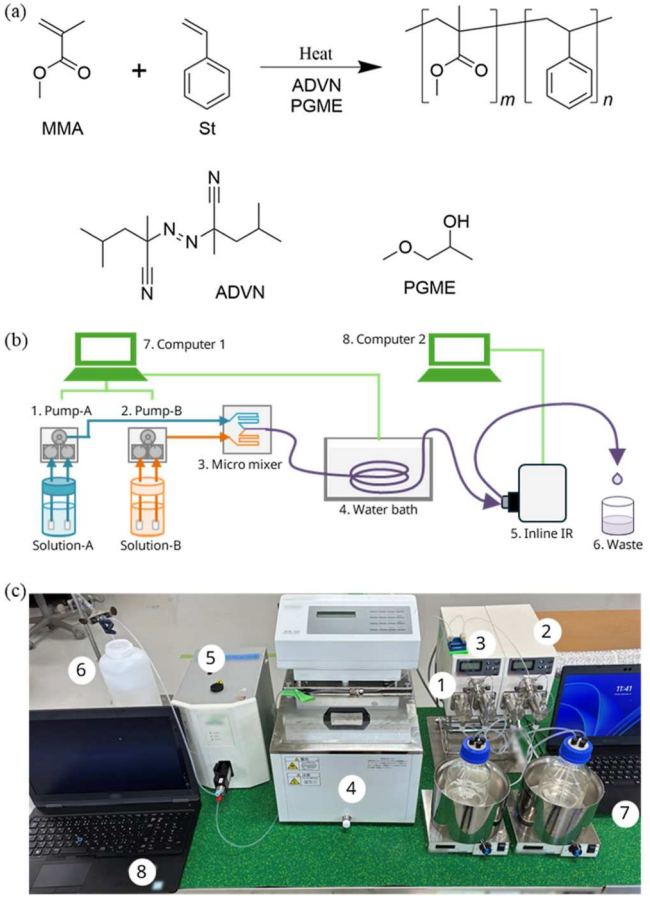


**Figure 2.** Overview of chemistry and setup. (a) Free-radical copolymerization scheme of styrene (St) and methyl methacrylate (MMA); structural formulas of the initiator 2,2′-azobis(2,4-dimethylvaleronitrile) (ADVN) and solvent propylene glycol monomethyl ether (PGME). Initiator loading (ADVN relative to total monomer) was nominally kept constant during the composition sweep. (b) Piping and device schematic (flow depicted left-to-right). Major components are labeled with indices (1−8). (c) Photograph of the experimental setup. White circled numbers correspond to the indices in panel b and enable one-to-one matching between the schematic and the photo.

0.75 mL min$^{-1}$ (Figure 3). The effective reactor volume was 31.4 mL; the residence time at 1.5 mL min$^{-1}$ total flow is 20.9 min. Temperatures were set to 25 °C (unreacted reference), 70, 80, and 90 °C. Runs at 60 °C yielded low conversion and lower information content for the present analysis; they are therefore excluded from the main analysis and shown only as an exploratory case in the Supporting Information. The zigzag program was used to sample similar composition regions during both increasing and decreasing feed-ratio trends within a single run; this design was intended to reduce sensitivity to systematic one-directional sweep bias, although it was not intended to provide an explicit correction for residence-time-distribution or flow-dispersion effects.

## 2.5. Inline ATR-FTIR Measurements and Flow-Cell Configuration

IR spectra were acquired every 15 s. Instrument default settings were used otherwise: resolution 8 cm$^{-1}$, spectral range 4000−600 cm$^{-1}$, 50 scans, gain 1×. The baseline was recorded in air. No spectral preprocessing was applied. Because small nitrogen bubbles can form from initiator decomposition at 90 °C, we adopted an upflow configuration (flow from the lower to the upper port of the flow module) to suppress bubble holdup. No back-pressure regulator was used.

## 2.6. UHPLC and SEC Measurements

Ten points were sampled offline from each run. The first sample was taken 10 min before the start of the zigzag feed-ratio sweep, and then at 20 min intervals. UHPLC used a photodiode array (PDA) detector with DMF as internal standard, detecting each component at a single wavelength appropriate to that analyte (St: 254 nm; MMA: 217 nm; DMF: 211 nm).

The mobile phase consisted of HPLC-grade water (Sigma-Aldrich) and HPLC-grade acetonitrile (FUJIFILM Wako Pure Chemical Corporation). The gradient started at acetonitrile: water = 45:55, changed linearly to 50.7:49.3 at 1.5 min, then linearly to 100:0 3 min later, and was held to 3.5 min. To prevent polymer blockage, a 1 min postrun wash with tetrahydrofuran (THF; Nacalai Tesque, stabilized with 2,6-di*tert*-butyl-4-methylphenol, approximately 250 ppm) was applied, followed by a return to the initial 45:55 composition. Column temperature and related settings were 40 °C.

For UHPLC sample preparation, the internal-standard stock solution was dimethylformamide (DMF; Nacalai Tesque, Special grade) at 0.45 wt % in THF (Nacalai Tesque, stabilized with 2,6-di*tert*-butyl-4-methylphenol ≈250 ppm). Samples underwent two-stage dilution prior to injection: first 50× with the internal-standard solution, then a further 50× with THF of the same specification.

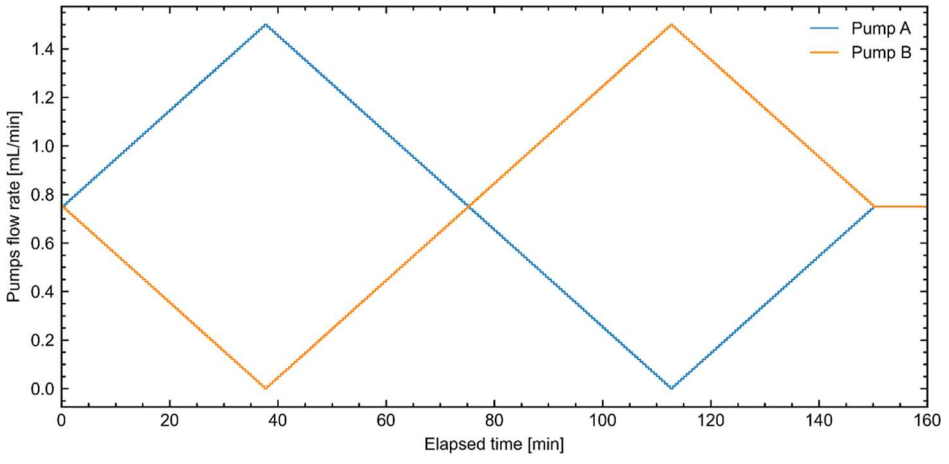


**Figure 3.** Overview of the zigzag flow-rate program used to sweep the styrene/MMA feed ratio. The combined flow rate of pumps (A) (St solution with ADVN) and (B) (MMA solution with ADVN) was kept at 1.5 mL min$^{-1}$, starting from 0.75/0.75 mL min$^{-1}$ and incrementing/decrementing by 0.01 mL min$^{-1}$ every 0.5 min. The direction reversed at 1.5/0 and 0/1.5 mL min$^{-1}$, and the program ended upon returning to the initial 0.75/0.75 mL min$^{-1}$





https://doi.org/10.1021/acsomega.6c06915
ACS Omega 2026, 11, 45574−45587

Calibration curves for St, MMA, and DMF were prepared at 5, 10, 25, 50, 75, and 100 ppm and fitted with quadratics.

SEC (GPC) measurements were performed on the same platform using a TSKgel SuperHM-M column (6.0 mm I.D. × 15 cm, 3 $\mu$m) with THF (Nacalai Tesque, stabilized with 2,6-di*tert*-butyl-4-methylphenol ≈250 ppm) as the eluent at 0.6 mL $min^{-1}$ and 40 °C, with refractive-index detection (RID). Number-average ($M_n$) and weight-average ($M_w$) molar masses were calculated versus polystyrene standards. The SEC calibration curve was constructed using 11 polystyrene standards spanning approximately $M_p = 0.58 \times 10^3 - 2.33 \times 10^6$ g $mol^{-1}$ (Shodex, STANDARD SL-105 and SM-105, vendor nominal values; full list provided in the SI, Table S7). The reported $M_n$ and $M_w$ values are provided only to confirm polymer formation and to indicate the molar-mass regime under the present conditions; they were not used for the reactivity-ratio estimation or composition calculations. SEC samples were analyzed after single-stage dilution with the same THF.

## 2.7. Core Data-Analysis Workflow

**2.7.1. Cross-Validated Lasso Model for Spectra-to-Concentration Mapping.** Two Lasso regression models were trained to map ATR-FTIR spectra to styrene (St) and methyl methacrylate (MMA) concentrations, with the regularization parameter selected by 5-fold cross-validation (scikit-learn v1.6.1). Features were all wavenumber points; StandardScaler in scikit-learn was applied for preprocessing. The final models were fitted on all 40 UHPLC−IR calibration pairs (10 per run at 25, 70, 80, and 90 °C). Model performance and representative reconstructions are reported in Section 3.1. The fit metrics reported for the final full-data models are calibration-fit diagnostics rather than external test statistics. Residual-based uncertainty estimation is described separately in Section 2.7.2.

**2.7.2. Residual-Based Uncertainty Estimation from Interior-Anchor Leave-One-Out Analysis.** Concentration-prediction uncertainty for within-run interpolation was estimated by leave-one-out analysis using only the interior anchors. For each of the four runs, the two end anchors were excluded from the validation pool, and the remaining eight interior anchors were held out one at a time, giving 32 hold-out cases in total. In each case, the Lasso models were retrained on the remaining 39 anchor points and used to predict the held-out styrene and MMA concentrations. The resulting hold-out residuals were then used to estimate monomer-specific Gaussian perturbation widths, $\sigma_{St}$ and $\sigma_{MMA}$. These $\sigma$ values were used as residual-based uncertainty estimates for the reconstructed concentration trajectories and were propagated in the subsequent Monte Carlo analysis described in Section 2.7.5.

**2.7.3. Construction of Finite-Conversion trajectory Variables from Time-Series Data.** Time-series monomer concentrations predicted by the Lasso models (Section 2.7.1) were converted to mole-fraction and conversion variables used to construct finite-conversion copolymerization trajectories. To enforce physical bounds, composition variables were clipped to the admissible interval [0, 1] (values <0 set to 0; values >1 set to 1). For this binary system, normalization was enforced by setting $f_2 = 1 - f_1$ and $F_{2,cum} = 1 - F_{1,cum}$ at each time point.

In this work, we denote the predicted time-series molar concentrations of styrene and MMA as $c_1(t)$ and $c_2(t)$. Here, $c_{i,ref}(t)$ denotes the unreacted reference trajectory at 25 °C, and $c_{i,rxn}(t)$ denotes the aligned reacting trajectory at the target temperature. The reference monomer composition was computed from the unreacted reference (25 °C) at each time point as

$$f_1(t) = c_{1,ref}(t)/(c_{1,ref}(t) + c_{2,ref}(t)) \quad (1)$$

In contrast, $F_{1,cum}(t)$ was computed from monomer consumption relative to the same reference trajectory, using

$$\Delta c_i(t) = \max(0, c_{i,ref}(t) - c_{i,rxn}(t)) \quad (2)$$

and

$$F_{1,cum}(t) = \Delta c_1(t)/(\Delta c_1(t) + \Delta c_2(t)) \quad (3)$$

Thus, $F_{1,cum}(t)$ is a consumption-based cumulative copolymer-composition proxy at the reactor outlet rather than a strictly differential instantaneous copolymer composition. The total conversion was computed as

$$X_{tot}(t) = (\Delta c_1(t) + \Delta c_2(t))/(c_{1,ref}(t) + c_{2,ref}(t)) \quad (4)$$

The corresponding $X_{tot}(t)$ and $F_{1,cum}(t)$ profiles are presented in Section 3.2. The reconstructed $F_{1,cum}(t)$ represents this consumption-based outlet composition proxy at the reactor outlet. Therefore, the reactivity-ratio estimation was performed using $f_1(t)$, $X_{tot}(t)$, and $F_{1,cum}(t)$ together in the Skeist-type finite-conversion fitting described in Section 2.7.4, rather than by directly fitting $F_{1,cum}(t)$ to an instantaneous composition equation. Temporal alignment, additional index shifting, and trimming were applied post hoc to ensure consistent correspondence between the reference and reaction trajectories; an overview is provided here, and implementation details are provided in the Supporting Information (Section S3 and Figure S1).

**2.7.4. Skeist-Type Finite-Conversion Reactivity-Ratio Fitting.** Reactivity-ratio estimation was performed using a Skeist-type finite-conversion terminal-model formulation.[6] This formulation was used because the experimentally reconstructed $F_{1,cum}(t)$ values in the present workflow correspond to cumulative consumption-based outlet composition proxies at finite $X_{tot}(t)$, rather than strictly differential instantaneous copolymer compositions. A direct nonlinear fit of the Mayo−Lewis equation to these $F_{1,cum}(t)$ values would therefore not be consistent with the observable. The Skeist-type calculation allows the Mayo−Lewis equation to be used locally as the instantaneous terminal-model composition relation while explicitly accounting for composition drift up to each observed conversion.

Reactivity ratios were defined under the terminal model as

$$r_1 = \frac{k_{11}}{k_{12}} \quad (5)$$

$$r_2 = \frac{k_{22}}{k_{21}} \quad (6)$$

where $k_{ab}$ denotes the propagation rate constant for a radical bearing terminal unit $a$ reacting with monomer $b$. In this study, monomer 1 corresponds to styrene and monomer 2 to methyl methacrylate. The Mayo−Lewis equation was used as the instantaneous composition relation

$$F_1^{inst}(f_1; r_1, r_2) = \frac{r_1 f_1^2 + f_1 f_2}{r_1 f_1^2 + 2 f_1 f_2 + r_2 f_2^2} \quad (7)$$

where $f_2 = 1 - f_1$. In the present analysis, this equation was not fitted directly to the $F_{1,cum}(t)$ proxy. Instead, it was used as the instantaneous composition relation embedded in a Skeist-type finite-conversion calculation.

For each data point $i$, the finite-conversion calculation was initialized using the reference monomer composition obtained from the aligned 25 °C trajectory. The residual monomer amounts, $n_{1,i}$ and $n_{2,i}$, were treated as normalized molar amounts and initialized such that $n_{1,i}(0) + n_{2,i}(0) = 1$

$$n_{1,i}(0) = f_{1,i}^{ref}, \qquad n_{2,i}(0) = 1 - f_{1,i}^{ref} \quad (8)$$

Here, $f_{1,i}^{ref}$ denotes the reference styrene mole fraction at data point $i$. During numerical integration, the residual monomer composition was updated from the remaining monomer amounts as

$$f_{1,i}(\xi) = \frac{n_{1,i}(\xi)}{n_{1,i}(\xi) + n_{2,i}(\xi)} \quad (9)$$

where $\xi$ denotes the integration coordinate corresponding to total fractional monomer consumption, ranging from 0 to the observed $X_{tot,i}$. At each integration step, $F_1^{inst}$ was calculated using eq 7, and the decrease in total monomer amount was apportioned according to the instantaneous copolymer composition until the prescribed total





https://doi.org/10.1021/acsomega.6c06915
ACS Omega 2026, 11, 45574−45587

conversion $X_{tot,i}$ was reached. The calculated monomer consumptions were then obtained as

$$\Delta n_{1,i}^{calc} = n_{1,i}(0) - n_{1,i}(X_{tot,i}),$$
$$\Delta n_{2,i}^{calc} = n_{2,i}(0) - n_{2,i}(X_{tot,i}) \quad (10)$$

The Skeist-type cumulative predicted composition for data point $i$ was defined from these calculated consumptions as

$$F_{1,cum,i}^{Skeist} = \frac{\Delta n_{1,i}^{calc}}{\Delta n_{1,i}^{calc} + \Delta n_{2,i}^{calc}} \quad (11)$$

thus, $F_{1,cum,i}^{Skeist}$ is a cumulative composition prediction calculated from $f_{1,i}^{ref}$, $X_{tot,i}$, $r_1$, and $r_2$ through the numerical integration, rather than an instantaneous $F_1^{inst}(f_1)$ value. Best-fit values of $r_1$ and $r_2$ were obtained by nonlinear least-squares minimization of

$$RSS(r_1, r_2) = \sum_i [F_{1,cum,i}^{obs} - F_{1,cum,i}^{Skeist}(f_{1,i}^{ref}, X_{tot,i}; r_1, r_2)]^2 \quad (12)$$

where $F_{1,cum,i}^{obs}$ denotes the observed consumption-based $F_{1,cum}$ proxy for data point $i$.The optimization was carried out in $\log_{10} r_1$ and $\log_{10} r_2$ space to enforce positive reactivity ratios. Numerical integration used $N_{steps}$ = 100, which was sufficient based on the convergence assessment provided in the Supporting Information. The fitted values are interpreted as apparent finite-conversion reactivity-ratio estimates under the present flow and analysis workflow.

**2.7.5. Monte Carlo Propagation of Concentration-Prediction Uncertainty.** The concentration-prediction uncertainty estimated in Section 2.7.2 was propagated to downstream variables by Monte Carlo simulation. Gaussian perturbations with widths $\sigma_{St}$ and $\sigma_{MMA}$ were added to the full-data predicted styrene and MMA concentration trajectories, and 500 perturbed trajectory sets were generated. For each perturbed set, $X_{tot}(t)$, $F_{1,cum}(t)$, and the finite-conversion reactivity ratio estimates $r_1$ and $r_2$ were recomputed using the same Skeist-type fitting procedure described in Section 2.7.4. The resulting ensembles were used to evaluate how pointwise concentration-prediction uncertainty is transferred to the derived copolymerization variables and Skeist-type apparent reactivity-ratio estimates.

### 2.8. Sensitivity and Robustness Analyses

The following analyses were performed to examine the robustness of the workflow and the sensitivity of the reported reactivity-ratio estimates.

**2.8.1. Anchor-Removal Analysis.** Sensitivity to sparse-anchor removal was examined by removing two contiguous UHPLC anchors simultaneously from each of the four runs (25, 70, 80, and 90 °C), giving five nonoverlapping removal patterns in total. For each pattern, the Lasso models were retrained on the remaining 32 anchor points, the dense IR-assisted trajectories were reconstructed, and the apparent finite-conversion reactivity ratios were re-estimated using the same Skeist-type fitting procedure. In parallel, apparent finite-conversion reactivity ratios were also re-estimated from the corresponding reduced UHPLC-only anchor sets using the Skeist-type fitting procedure. The resulting method-specific $r_1$–$r_2$ clouds were compared with full-data estimates and with benchmark values from the literature.

**2.8.2. UHPLC-Only Subset Dependence Analysis.** UHPLC-only subset dependence was examined by enumerating all combinations of $n$ = 6 and 8 anchors from the ten available UHPLC points at each temperature. The $n$ = 10 case was treated as the full UHPLC-only estimate. For each subset, $f_1$, $X_{tot}$, $F_{1,cum}$, and the apparent finite-conversion $r_1$ and $r_2$ values were recomputed using the Skeist-type fitting procedure.

## 3. RESULTS AND DISCUSSION

### 3.1. Lasso-Based Concentration Mapping

The gradient flow program (Figure 3) swept the feed ratio continuously while inline ATR-FTIR acquired spectra every 15 s, yielding several hundred to ~740 spectra in a single run at each temperature. We used ten UHPLC points per run (40 total) as calibration to train cross-validated sparse Lasso models that map spectra to concentrations. A consolidated list of sampling times (referenced to the start of the zigzag feed ratio sweep), UHPLC-determined mass fractions (St/MMA), and SEC-determined $M_n$ and $M_w$ is provided in Table 1. Here, MAE and RMSE denote the mean absolute error and root-mean-square error, respectively. Residual-vs-Observed plots (Figure 4a,b) showed near-zero bias and narrow error bands across the calibration range: for the St [wt/wt] model ($\alpha$ = 6.93 × $10^{-5}$), $R^2$ = 0.9996, MAE = 0.0008 [wt/wt], RMSE =

**Table 1. Summary of Experimental Conditions, Sampling Times, and Analytical Results**[a]

| temperature [°C] | elapsed time [sec] | St [wt %] | MMA [wt %] | $M_n$ [g mol$^{-1}$] | $M_w$ [g mol$^{-1}$] |
|---|---|---|---|---|---|
| 25 | 1295 | 10.0 | 9.64 | - | - |
| 25 | 2474 | 14.6 | 5.49 | - | - |
| 25 | 3682 | 19.8 | 0.67 | - | - |
| 25 | 4881 | 15.3 | 4.33 | - | - |
| 25 | 6082 | 10.2 | 9.42 | - | - |
| 25 | 7323 | 4.87 | 15.2 | - | - |
| 25 | 8525 | 0.50 | 20.0 | - | - |
| 25 | 9686 | 5.19 | 15.0 | - | - |
| 25 | 10920 | 9.83 | 9.95 | - | - |
| 25 | 12085 | 10.1 | 10.0 | - | - |
| 70 | 1181 | 6.49 | 6.43 | 1567 | 3353 |
| 70 | 2383 | 11.21 | 3.63 | 1449 | 3060 |
| 70 | 3593 | 15.54 | 0.39 | 1374 | 2836 |
| 70 | 4780 | 11.29 | 3.15 | 1478 | 3139 |
| 70 | 5991 | 6.58 | 6.65 | 1611 | 3451 |
| 70 | 7187 | 2.40 | 9.35 | 1726 | 3819 |
| 70 | 8382 | 0.05 | 7.80 | 1445 | 3819 |
| 70 | 9586 | 2.86 | 9.59 | 1699 | 3769 |
| 70 | 10782 | 6.72 | 7.07 | 1601 | 3432 |
| 70 | 11979 | 6.67 | 6.91 | 1592 | 3397 |
| 80 | 1135 | 7.44 | 7.45 | 1761 | 3539 |
| 80 | 2341 | 11.43 | 4.41 | 1626 | 3253 |
| 80 | 3537 | 16.03 | 0.59 | 1547 | 2981 |
| 80 | 4737 | 12.74 | 3.14 | 1558 | 3088 |
| 80 | 5943 | 7.94 | 7.02 | 1704 | 3389 |
| 80 | 7140 | 3.38 | 10.55 | 1892 | 3864 |
| 80 | 8338 | 0.06 | 9.56 | 1959 | 4610 |
| 80 | 9540 | 2.87 | 10.69 | 1988 | 3976 |
| 80 | 10751 | 7.42 | 7.60 | 1705 | 3461 |
| 80 | 11963 | 7.44 | 7.51 | 1691 | 3381 |
| 90 | 1221 | 8.53 | 8.30 | 2289 | 4505 |
| 90 | 2410 | 12.76 | 4.60 | 2085 | 4041 |
| 90 | 3612 | 17.84 | 0.52 | 2001 | 3779 |
| 90 | 4811 | 13.74 | 3.64 | 1998 | 3865 |
| 90 | 6011 | 8.77 | 8.09 | 2323 | 4423 |
| 90 | 7217 | 3.85 | 12.08 | 2692 | 5354 |
| 90 | 8419 | 0.15 | 13.32 | 3428 | 7415 |
| 90 | 9610 | 3.92 | 12.26 | 2787 | 5503 |
| 90 | 10813 | 8.31 | 8.28 | 2416 | 4585 |
| 90 | 12018 | 8.35 | 8.21 | 2375 | 4544 |

[a]Elapsed time is referenced to the start of the zigzag feed-ratio sweep. For each sample, the table lists temperature, elapsed time, UHPLC-determined mass fractions of styrene (St) and methyl methacrylate (MMA), and SEC-determined number-average ($M_n$) and weight-average ($M_w$) molar masses.





https://doi.org/10.1021/acsomega.6c06915
ACS Omega 2026, 11, 45574−45587

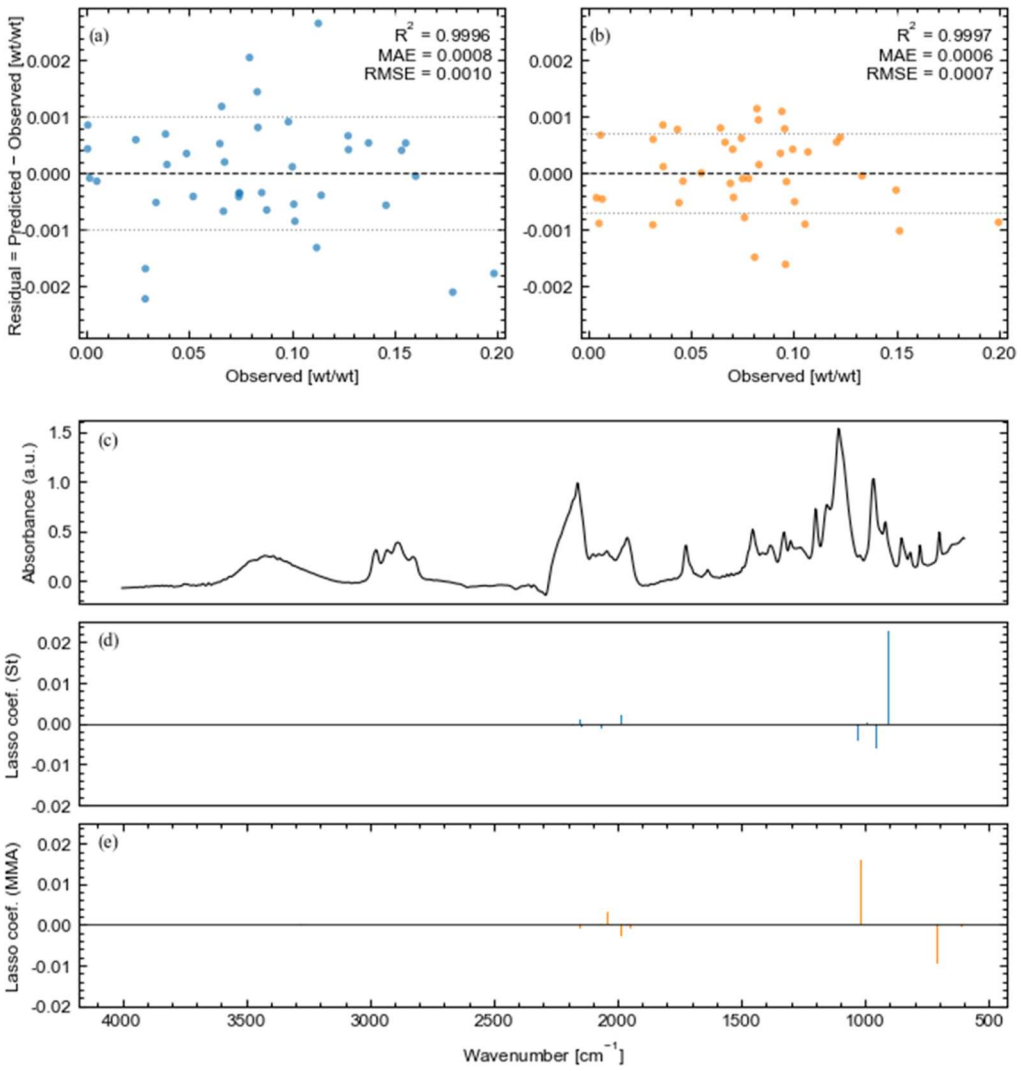


**Figure 4.** Residual diagnostics and feature visualization for cross-validated Lasso models fitted to all 40 UHPLC-IR calibration pairs. (a) Residuals (Predicted−Observed) vs Observed for styrene (St) [wt/wt] with zero-residual line and ± RMSE guides. (b) Same for methyl methacrylate (MMA). (c) Representative ATR-FTIR spectrum (80 °C, 0.75/0.75 mL min$^{-1}$). (d) Lasso coefficients for St. (e) Lasso coefficients for MMA.

0.0010 [wt/wt]; for the MMA [wt/wt] model ($\alpha$ = 4.01 × 10$^{-5}$), $R^2$ = 0.9997, MAE = 0.0006 [wt/wt], RMSE = 0.0007 [wt/wt]. These diagnostics are computed on the 40 UHPLC-IR calibration points used to train the models.

To assess interpretability, we inspected the learned Lasso coefficients (Figure 4d,e), which concentrated on chemically consistent bands. With standard scaler preprocessing, coefficient signs can be interpreted directly. In the St model, aromatic out-of-plane C−H bending in the low wavenumber region (∼700−910 cm$^{-1}$, notably 906−910 cm$^{-1}$) contributed strongly and positively. In the MMA model, ester derived C−O/skeletal bands (∼1000−1100 cm$^{-1}$, around 1018 cm$^{-1}$) and contributions near 1300 cm$^{-1}$ were primary, with ester C═O stretching (∼1730 cm$^{-1}$) selected as a secondary contributor, consistent with MMA-specific functional groups. Conversely, the St model selected ∼1730 cm$^{-1}$ with a negative coefficient, indicating an inverse association with increases in MMA (carbonyl intensity). Although the solvent PGME C−O−C region (∼1000−1150 cm$^{-1}$) overlaps with MMA's C−O, sparse regression separated mixed contributions via positive/negative coefficients. These patterns support that the models capture the low-rank, approximately linear physicochemical structure of absorbance vs concentration rather than overfitting noise.

The trained models were then applied to all inline spectra to reconstruct St and MMA wt/wt concentrations at each time point (Figure 5), enabling dense trajectory reconstruction and downstream finite-conversion trajectory analysis with minimal offline workload.

### 3.2. Dense Trajectory Reconstruction and Derived Variables

The reconstructed St and MMA concentration trajectories shown in Figure 5 were then converted into the derived variables $X_{tot}(t)$ and $F_{1,cum}(t)$ using the aligned 25 °C run as the unreacted reference. Figure 6 shows the resulting full-data trajectories for 70, 80, and 90 °C together with 5−95% uncertainty bands obtained by propagating the residual-based concentration-prediction uncertainty. Conversion increased systematically with temperature and reached maxima of 0.36 at 70 °C, 0.52 at 80 °C, and 0.62 at 90 °C, with median values of 0.15, 0.24, and 0.32, respectively. The $X_{tot}$ bands remained relatively narrow across most of the trajectories. The $F_{1,cum}$ bands were also compact over the interior composition range, but widened near low-contrast and boundary regions, where




https://doi.org/10.1021/acsomega.6c06915
ACS Omega 2026, 11, 45574−45587

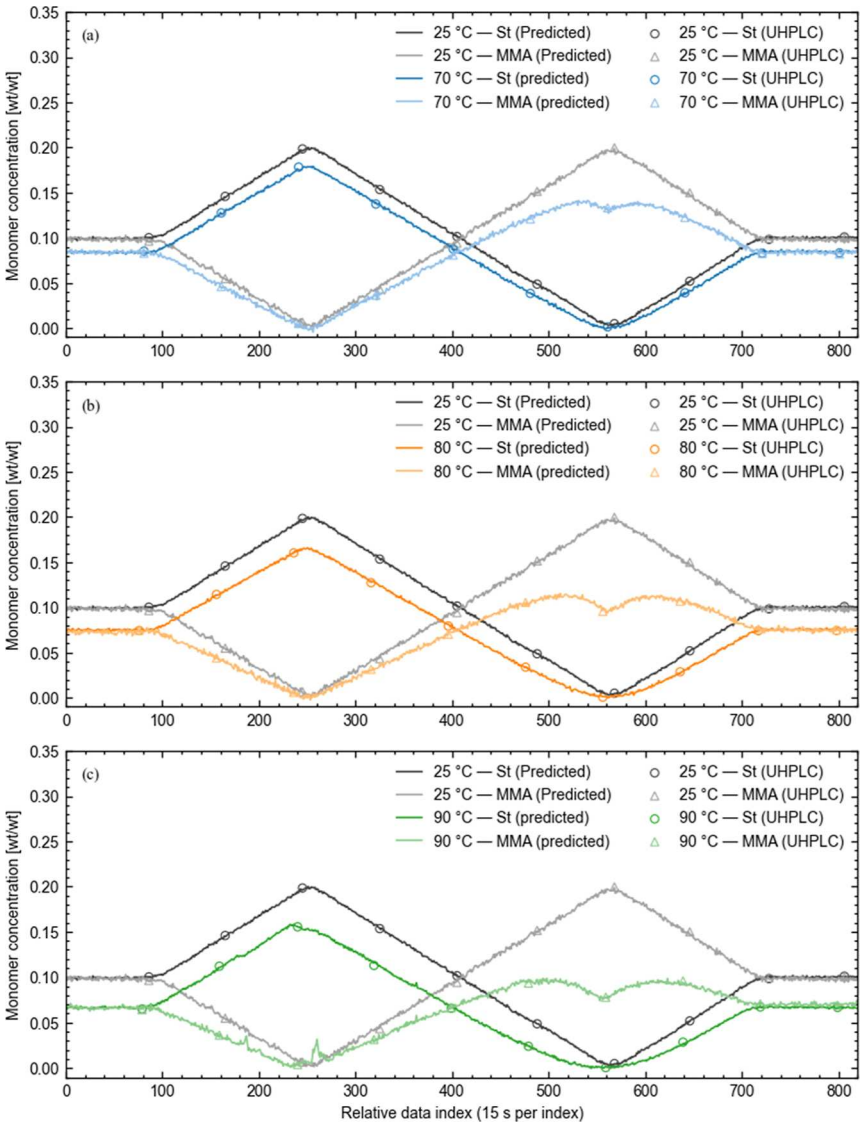


**Figure 5.** Comparison between unreacted (25 °C) and reaction conditions with overlaid prediction curves and UHPLC references. (a) Comparison of St/MMA concentration trajectories (w/w) at 25 °C (unreacted) and 70 °C. (b) Comparison at 25 °C (unreacted) and 80 °C. (c) Comparison at 25 °C (unreacted) and 90 °C. All panels are plotted on a normalized relative index (15 s per index), overlaying predictions (solid lines) and UHPLC measurements (scatter).

the cumulative composition proxy becomes more sensitive to small concentration perturbations.

At each time point, $f_1(t)$, taken from the aligned 25 °C reference composition, was combined with the corresponding $X_{tot}(t)$ and $F_{1,cum}(t)$ value from the reacting run to construct dense finite-conversion copolymerization trajectories. These three variables serve as the inputs to the Skeist-type finite-conversion fitting described in Section 3.3. The trajectories span the full composition range traversed during a single zigzag run at each temperature and provide the basis for the apparent reactivity-ratio analysis discussed below.

### 3.3. Skeist-type Finite-Conversion Reactivity-Ratio Estimation

The dense $f_1(t)$, $X_{tot}(t)$, and $F_{1,cum}(t)$ trajectories were analyzed using the Skeist-type finite-conversion terminal-model formulation described in Section 2.7.4. In this formulation, the Mayo−Lewis equation is used only as the instantaneous composition relation, while the fitted observable is the cumulative composition predicted after integration to the observed total conversion. This treatment explicitly accounts for composition drift over the finite conversion interval associated with each trajectory point.

Figure 7a−c shows the observed dense trajectories and the corresponding point-wise Skeist cumulative predictions for 70, 80, and 90 °C. The predicted values are denoted as $F_{1,cum}^{Skeist}$ and were calculated at each data point using the fitted $r_1$ and $r_2$ values together with the corresponding $f_1(t)$ and $X_{tot}(t)$. Thus, these plotted values are trajectory-point-specific finite-conversion cumulative predictions rather than a universal instantaneous $F_1^{inst}(f_1)$ curve. Figure 7d compares the temperature-specific $F_{1,cum}^{Skeist}$ predictions with the global prediction obtained by combining the inline-derived trajectory points from 70−90 °C.

The Skeist-type finite-conversion analysis of the full-data IR-assisted trajectories gave apparent finite-conversion estimates of $r_1$ = 0.33, 0.44, and 0.48 and $r_2$ = 0.39, 0.44, and 0.42 at 70, 80, and 90 °C, respectively. These estimates are used as the full-data references for the uncertainty propagation and




https://doi.org/10.1021/acsomega.6c06915
ACS Omega 2026, 11, 45574−45587

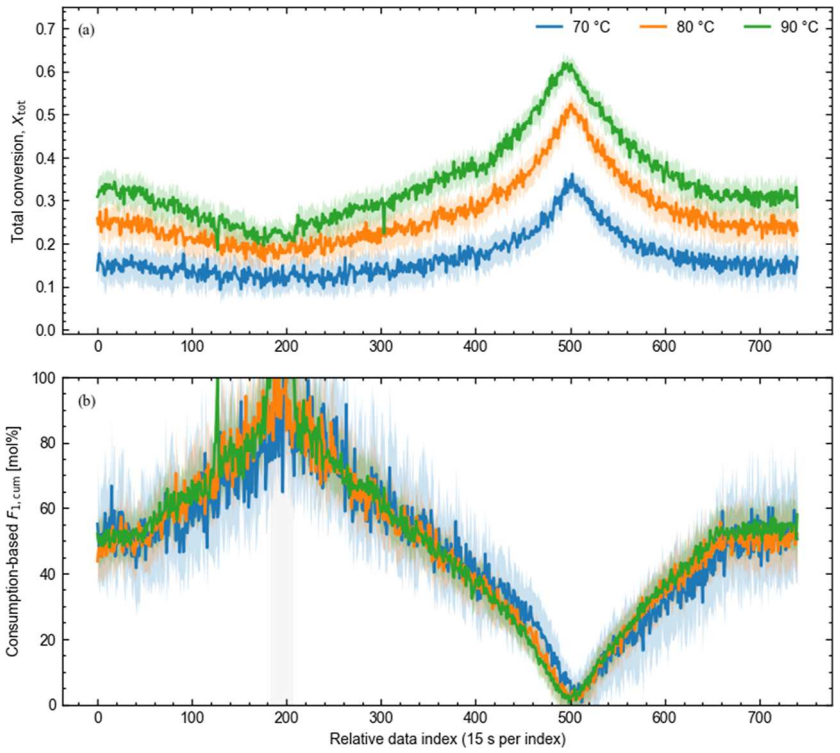


**Figure 6.** Uncertainty overlays for $X_{tot}$ and$F_{1,cum}$ from the Monte Carlo perturbation analysis. (a) Full-data $X_{tot}$ trajectories for 70, 80, and 90 °C overlaid with Monte Carlo 5−95% uncertainty bands generated from Gaussian concentration perturbations using leave-one-out residual-based $\sigma$ values. (b) Full-data consumption-based $F_{1,cum}$ trajectories for 70, 80, and 90 °C overlaid with Monte Carlo 5−95% uncertainty bands. For $F_{1,cum}$, the shaded bands are emphasized over the interior composition region, and gray spans highlight low-contrast or boundary regions where the ratio-based proxy becomes more sensitive.

robustness analyses below. They are interpreted as apparent finite-conversion reactivity-ratio estimates under the present flow and analysis workflow, rather than as strict low-conversion differential reactivity ratios.

### 3.4. Residual-Based Uncertainty Propagation and Monte Carlo Distributions

To evaluate the contribution of pointwise concentration-prediction error, perturbation widths $\sigma$ were estimated from interior-anchor leave-one-out residuals and propagated through the full-data reconstruction and Skeist-type fitting workflow by Monte Carlo simulation (500 replicates). The resulting $r_1-r_2$ Monte Carlo clouds are shown in Figure 8, and the corresponding summaries are given in Table 2.

In all three temperature cases, the Monte Carlo clouds are relatively compact and remain centered near the full-data IR-assisted estimates. This suggests that the full-data IR-assisted fits are internally consistent with respect to realistic concentration-prediction noise. At the same time, the compactness of these clouds suggests that pointwise prediction noise alone is not enough to explain the larger method-dependent offsets and subset sensitivities observed in the robustness analyses below.

Complementary trajectory-level perturbation results for $X_{tot}$ and $F_{1,cum}$ are shown in Figure 6. In particular, the consumption-based $F_{1,cum}$ proxy shows locally increased sensitivity near low-contrast or boundary regions, which is consistent with its ratio-based construction from aligned reference and reacting trajectories.

### 3.5. Block-Removal Robustness and Benchmark Comparison

Robustness was assessed by a five-block anchor-removal experiment. Two contiguous UHPLC anchors were removed simultaneously from each of the four runs, the Lasso models were retrained on the remaining 32 anchors, and the dense IR-assisted trajectories were reconstructed. Apparent finite-conversion reactivity ratios were then re-estimated using the same Skeist-type fitting procedure. In parallel, apparent finite-conversion reactivity-ratio estimates were also obtained from the corresponding reduced UHPLC-only anchor sets. The resulting $r_1-r_2$ clouds are compared with full-data estimates and benchmark literature values in Figure 9.

Figure 9 shows three main features. First, the IR-assisted and UHPLC-only block-removal clouds have a comparable spread, and dense inline reconstruction does not produce a marked reduction in variability. Second, both the IR-assisted and UHPLC-only full-data estimates remain within the broad benchmark literature cluster for St/MMA copolymerization. Third, the method-specific clouds are centered near their respective full-data estimates, showing that each workflow remains internally consistent under anchor removal.

The method-dependent offset is most evident at 70 °C, where the full-data IR-assisted estimate lies away from the corresponding UHPLC-only cloud. By contrast, the 80 and 90 °C results are more mutually consistent and remain broadly aligned with the literature cluster. These results show that dense inline reconstruction does not markedly narrow the spread of reactivity-ratio estimates under anchor removal, while still providing benchmark-consistent full-data estimates and dense composition mapping.





https://doi.org/10.1021/acsomega.6c06915
ACS Omega 2026, 11, 45574−45587

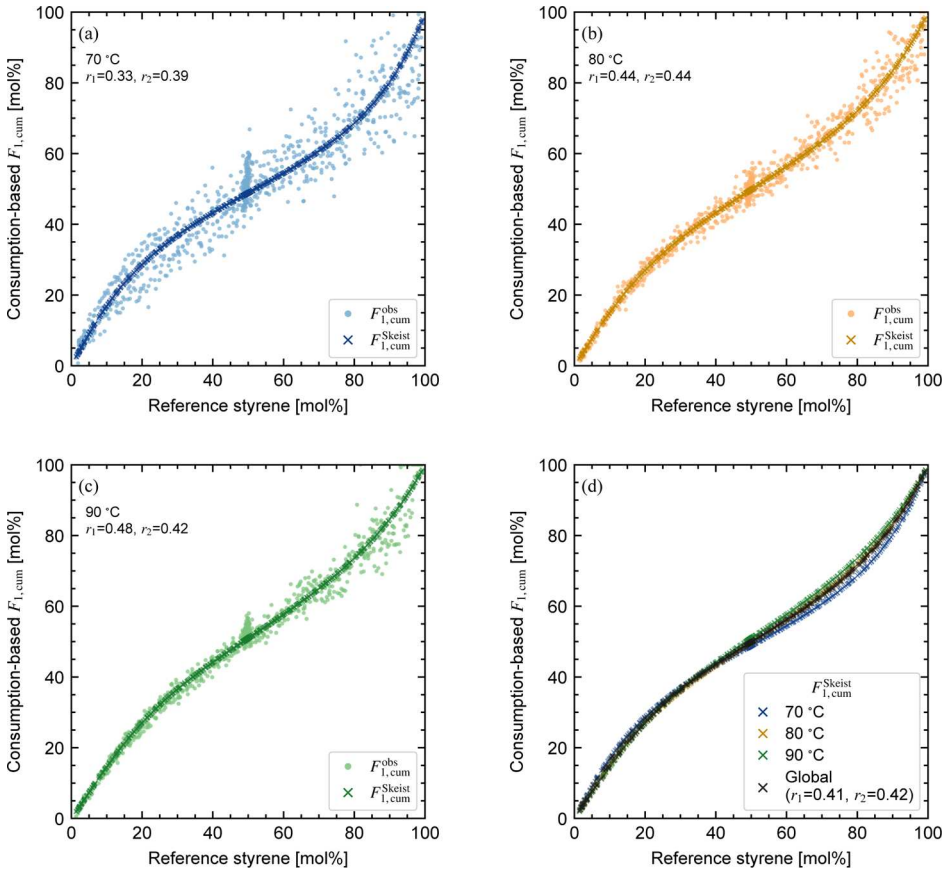


**Figure 7.** Observed finite-conversion trajectories and pointwise Skeist cumulative predictions constructed from full-data time-resolved trajectories. (a–c) Observed dense $f_1(t) - F_{1,cum}(t)$ trajectories and pointwise Skeist cumulative predictions at 70 °C, 80 °C, and 90 °C, respectively. Filled symbols show the observed consumption-based cumulative composition proxy, $F_{1,cum}^{obs}$, calculated from the aligned 25 °C reference and reacting trajectories. Cross markers show the corresponding pointwise Skeist cumulative predictions, $F_{1,cum}^{Skeist}$, calculated using the fitted $r_1$ and $r_2$ values at each data point's corresponding $f_1(t)$ and $X_{tot}(t)$. These predicted values are pointwise finite-conversion cumulative predictions and should not be interpreted as universal instantaneous Mayo–Lewis $F_1^{inst}(f_1)$ curves. (d) Overlay of the temperature-specific $F_{1,cum}^{Skeist}$ predictions and a global prediction obtained by combining the inline-derived trajectory points from 70–90 °C.

### 3.6. Sensitivity to Anchor Selection and Sparse-Data Subset Choice

The UHPLC-only Skeist-type apparent finite-conversion reactivity-ratio estimates were themselves dependent on subset choice (Figure S3 and Table S5). The subset clouds were broader for $n = 6$ than for $n = 8$ and narrowed as the number of retained anchors approached the full $n = 10$ UHPLC-only estimate. This behavior indicates that, under the present data density, sparse UHPLC-only fitting does not collapse to a uniquely stable reference point. Comparisons between the UHPLC-only and IR-assisted estimates should therefore be interpreted together with the subset sensitivity of the sparse reference itself.

### 3.7. Scope and Limitations

The present workflow is designed to reconstruct dense copolymerization trajectories from sparse offline anchors and correlated inline spectra under unified flow conditions. Its main value is efficient mapping of concentration evolution, conversion, and derived copolymerization variables across a broad composition sweep, together with residual-based uncertainty propagation. Finite-conversion effects and composition drift are explicitly incorporated through the Skeist-type fitting procedure. Nevertheless, the resulting reactivity-ratio values are best interpreted as apparent finite-conversion estimates obtained under the present flow and analysis workflow.

Several workflow-specific factors remain important for this interpretation. The fitted values depend on sparse-anchor placement, alignment between the reacting and reference runs, baseline differencing, and the consumption-based $F_{1,cum}$ proxy. In addition, the 2 mol % ADVN loading and the resulting low-molar-mass regime are part of the present flow-optimized conditions and form part of the context for interpreting the fitted values as condition-specific apparent estimates.

Low-conversion data remain useful as validation points and limiting cases for comparison. In the gradient-flow runs, conversion was not independently controlled across composition, and the high- and low-conversion regions depended strongly on monomer composition. Restricting the present dataset post hoc to low-conversion points would therefore truncate the accessible composition range unevenly and reduce the information content available for fitting, especially in sparse anchor-only cases. Accordingly, the main analysis used the full reconstructed finite-conversion trajectories, and the fitted $r_1$ and $r_2$ values are reported as apparent finite-conversion estimates obtained under the present flow and analysis workflow.

The 80 and 90 °C data sets provide the most stable overall behavior, with IR-assisted full-data estimates that remain




https://doi.org/10.1021/acsomega.6c06915
ACS Omega 2026, 11, 45574–45587

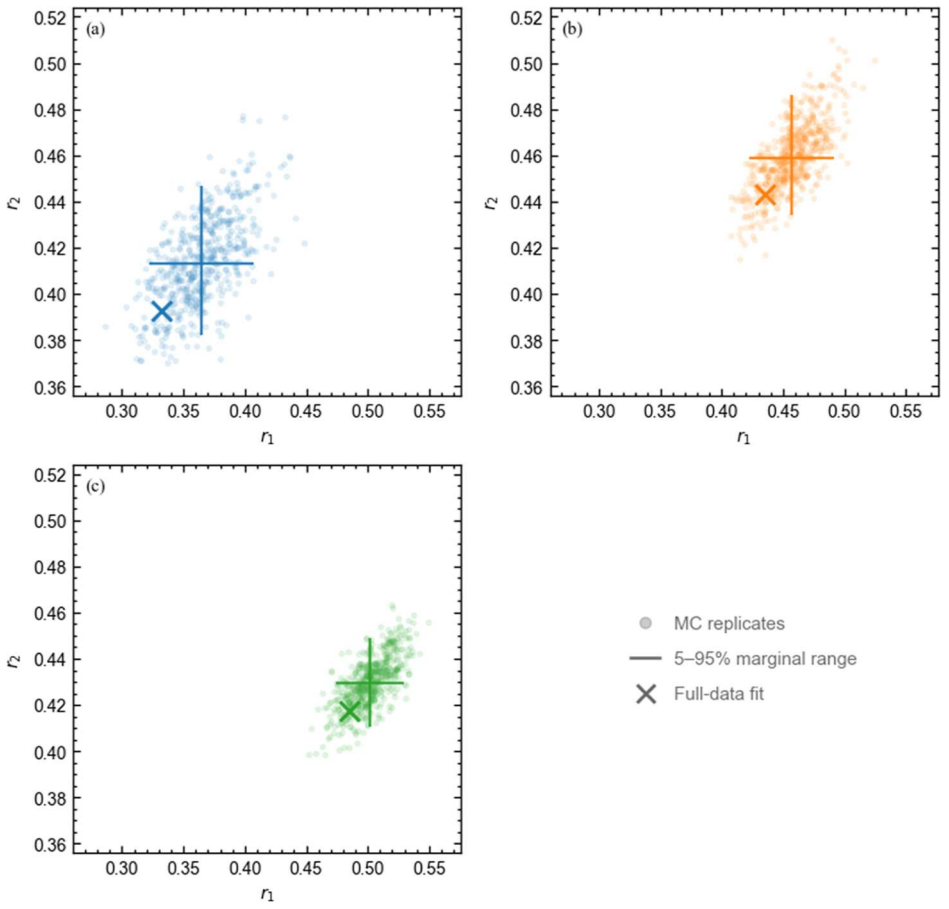


**Figure 8.** Monte Carlo propagation of concentration-prediction uncertainty to apparent finite-conversion reactivity-ratio estimates. (a–c) Temperature-specific $r_1$–$r_2$ distributions for 70, 80, and 90 °C, respectively, obtained by propagating Gaussian concentration perturbations through the full-data IR-assisted workflow and refitting each replicate using the Skeist-type finite-conversion procedure (500 replicates). The perturbation widths $\sigma$ for styrene and methyl methacrylate concentrations were estimated from interior-anchor leave-one-out residuals, in which the two end anchors of each run were excluded from the validation pool and the remaining eight interior anchors were held out one at a time. Small circles denote Monte Carlo replicates, crosshairs indicate the marginal 5–95% ranges in $r_1$ and $r_2$, and "×" markers denote the corresponding full-data IR-assisted estimates. These distributions quantify the contribution of pointwise concentration-prediction noise to the apparent finite-conversion reactivity-ratio estimates.

**Table 2. Summary of Monte Carlo Perturbation Results for Skeist-type Apparent Finite-Conversion Reactivity-Ratio Estimates**[a]

| | $r_1$ | | | | | | $r_2$ | | | | | |
|---|---|---|---|---|---|---|---|---|---|---|---|---|
| temperature [°C] | full | $p_{05}$ | $p_{50}$ | $p_{95}$ | absolute deviation median | absolute deviation $p_{95}$ | full | $p_{05}$ | $p_{50}$ | $p_{95}$ | absolute deviation median | absolute deviation $p_{95}$ |
| 70 | 0.332 | 0.322 | 0.365 | 0.407 | 0.032 | 0.075 | 0.393 | 0.382 | 0.413 | 0.447 | 0.021 | 0.054 |
| 80 | 0.435 | 0.423 | 0.457 | 0.491 | 0.023 | 0.056 | 0.443 | 0.434 | 0.459 | 0.486 | 0.016 | 0.043 |
| 90 | 0.485 | 0.474 | 0.502 | 0.529 | 0.018 | 0.045 | 0.418 | 0.411 | 0.429 | 0.449 | 0.012 | 0.031 |

[a]Gaussian perturbations were applied to the full-data IR-assisted concentration trajectories using monomer-specific $\sigma$ values estimated from interior-anchor leave-one-out residuals, and $r_1$ and $r_2$ were recomputed using the Skeist-type fitting procedure. The table lists the full-data $r_1$ and $r_2$ values together with the 5th, 50th, and 95th percentiles of the Monte Carlo distributions, as well as the median and 95th-percentile absolute deviations from the corresponding full-data estimates.

broadly aligned with both the benchmark literature cluster and the corresponding reduced-data results. At 70 °C, a residual method-dependent offset remains, and this condition is therefore interpreted as the most sensitive low-information regime in the present data set. Future work should refine the lag and alignment treatments, implement conversion-controlled and conversion-matched designs that include both low-conversion validation points and deliberately varied finite-conversion trajectories to enable a more independent experimental assessment of workflow-specific effects, and extend the workflow to other monomer pairs and media.

The present trajectory alignment also does not explicitly model the full residence-time distribution of the tubular reactor or laminar-flow dispersion. Although the zigzag feed-composition program samples similar composition regions during both increasing and decreasing sweep directions, this design does not constitute an explicit RTD correction. Residual residence-time and flow-dispersion effects may





https://doi.org/10.1021/acsomega.6c06915
ACS Omega 2026, 11, 45574–45587

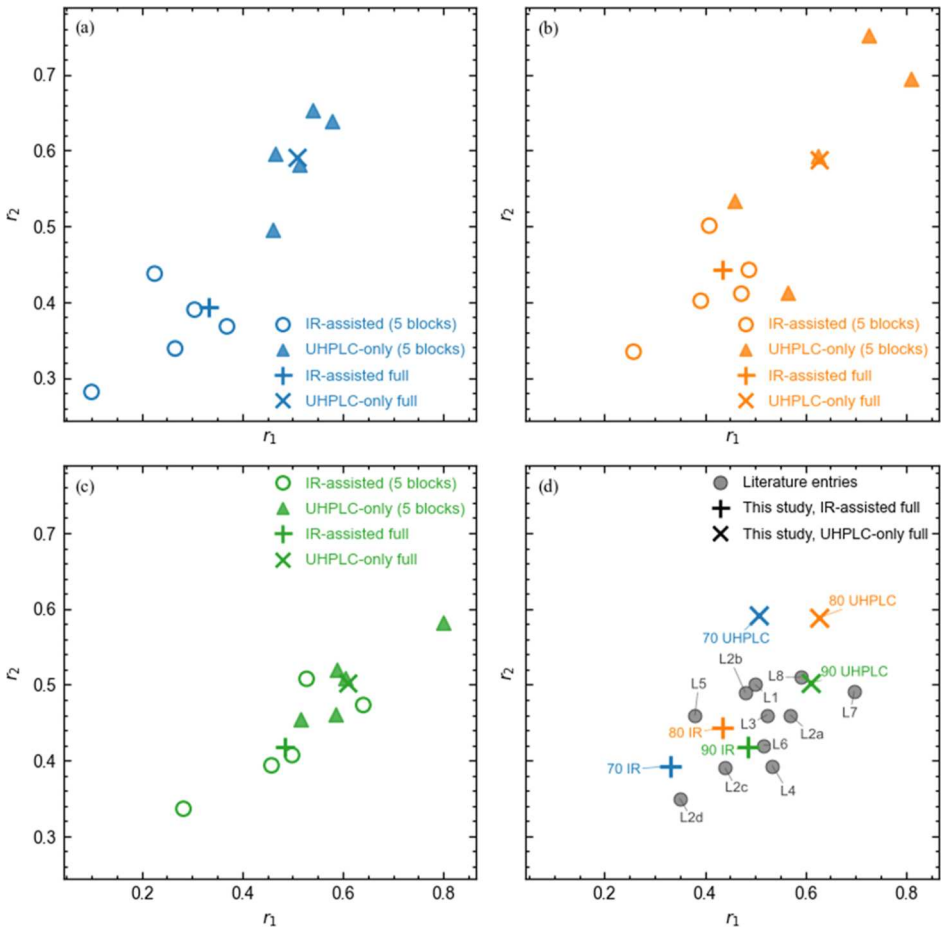


**Figure 9.** Block-removal robustness and benchmark comparison of apparent finite-conversion reactivity-ratio estimates. (a−c) Temperature-specific $r_1$−$r_2$ plots for 70, 80, and 90 °C, respectively, obtained from five nonoverlapping anchor-removal patterns. In each pattern, two contiguous UHPLC anchors were removed from each of the four runs (25, 70, 80, and 90 °C), the Lasso models were retrained on the remaining 32 anchors, the IR-assisted trajectories were reconstructed, and the apparent finite-conversion reactivity ratios were re-estimated using the Skeist-type finite-conversion procedure. Open circles denote IR-assisted reduced-data estimates, and filled triangles denote UHPLC-only reduced-data estimates. "+" and "×" markers indicate the corresponding full-data IR-assisted and UHPLC-only estimates, respectively. (d) Overlay of the full-data estimates with benchmark literature values for styrene/methyl methacrylate copolymerization compiled in Table S1. Gray circles denote literature values, and the labels identify the corresponding literature entries. The benchmark overlay is intended to provide broad literature context rather than an accuracy ranking among methods.

therefore remain and are included among the workflow-specific factors contributing to the apparent finite-conversion nature of the reported estimates.

## 4. CONCLUSIONS

We presented a workflow that combines gradient continuous-flow free-radical copolymerization, inline ATR-FTIR, and sparse linear regression to reconstruct dense concentration and composition trajectories from minimal offline quantitation. In the St/MMA system, more than 700 inline spectra acquired in a single run were anchored by only ten offline UHPLC measurements per temperature, enabling high-density reconstruction of $f_1(t)$, $X_{tot}(t)$, and consumption-based $F_{1,cum}(t)$ trajectories at 70, 80, and 90 °C. The final Lasso models showed calibration-fit diagnostics of $R^2 > 0.999$ and RMSE ≤0.0010 wt/wt for both monomers.

The reconstructed finite-conversion trajectories were analyzed using a Skeist-type finite-conversion terminal-model formulation, in which the Mayo−Lewis equation was used as the instantaneous composition relation. The maximum $X_{tot}$ values spanned 0.36−0.62, and the full-data IR-assisted estimates spanned $r_1$ = 0.33−0.48 and $r_2$ = 0.39−0.44, remaining within the broad range of benchmark literature values for this system. Residual-based Monte Carlo sampling showed that pointwise concentration-prediction uncertainty led to compact $r_1$−$r_2$ ensembles, whereas separate robustness analyses showed sensitivity to sparse-anchor selection, most notably at 70 °C.

Because the workflow uses finite-conversion trajectory data, aligned reference/reacting concentration differences, and a consumption-based $F_{1,cum}$ proxy, the reported values are interpreted as apparent finite-conversion reactivity-ratio estimates under the present experimental and analytical conditions. Overall, the method provides a practical route to dense, uncertainty-aware copolymerization-trajectory mapping from minimal offline quantitation and enables unified comparison across temperatures within a single flow-based framework. Future work will benefit from conversion-controlled and conversion-matched experimental designs that include both low-conversion validation points and deliberately varied finite-conversion trajectories, thereby enabling clearer




https://doi.org/10.1021/acsomega.6c06915
ACS Omega 2026, 11, 45574−45587

experimental separation of terminal-model parameters from workflow-specific effects.

## ■ ASSOCIATED CONTENT

### Data Availability Statement

The raw data and analysis code required to regenerate the processed concentration and composition trajectories and obtain the main apparent reactivity-ratio point estimates are made available on GitHub (https://github.com/Wa-Araki/gradient-flow-copolymerization) (libraries used: scikit-learn v1.6.1, SciPy v1.15.2, NumPy v2.2.3, pandas v2.2.3).

### Supporting Information

The Supporting Information is available free of charge at https://pubs.acs.org/doi/10.1021/acsomega.6c06915.

Additional details on trajectory alignment, concentration reconstruction, uncertainty propagation, block-removal and UHPLC-only subset analyses, exploratory 60 °C analysis, numerical convergence assessment, benchmark comparison, and supplemental figures and tables (PDF)

## ■ AUTHOR INFORMATION


### Corresponding Authors

**Tomoyuki Miyao** − *Graduate School of Science and Technology, Nara Institute of Science and Technology, Nara 630-0192, Japan; Data Science Center, Nara Institute of Science and Technology, Nara 630-0192, Japan;* orcid.org/0000-0002-8769-2702; Email: miyao@dsc.naist.jp

**Hiroharu Ajiro** − *Graduate School of Science and Technology, Nara Institute of Science and Technology, Nara 630-0192, Japan; Data Science Center and Medilux Research Center, Nara Institute of Science and Technology, Nara 630-0192, Japan;* orcid.org/0000-0003-4091-6956; Email: ajiro@ms.naist.jp

### Authors

**Araki Wakiuchi** − *JSR Corporation, Kawasaki, Kanagawa 210-0821, Japan; Graduate School of Science and Technology, Nara Institute of Science and Technology, Nara 630-0192, Japan*

**Aniruddha Nag** − *Graduate School of Science and Technology, Nara Institute of Science and Technology, Nara 630-0192, Japan;* orcid.org/0000-0002-1570-2262

**Swarit Jasial** − *Graduate School of Science and Technology, Nara Institute of Science and Technology, Nara 630-0192, Japan; Data Science Center, Nara Institute of Science and Technology, Nara 630-0192, Japan;* orcid.org/0000-0003-1415-8151

**Masashi Nakayama** − *Graduate School of Science and Technology, Nara Institute of Science and Technology, Nara 630-0192, Japan*

**Shogo Takasuka** − *Graduate School of Science and Technology, Nara Institute of Science and Technology, Nara 630-0192, Japan*

**Shigehito Asano** − *JSR Corporation, Yokkaichi, Mie 510-8552, Japan*

**Ryo Hashizume** − *JSR Corporation, Yokkaichi, Mie 510-8552, Japan*

**Miho Hatanaka** − *Department of Chemistry, Faculty of Science and Technology, Keio University, Yokohama, Kanagawa 223-8522, Japan; Institute for Molecular Science, Okazaki, Aichi 444-8585, Japan;* orcid.org/0000-0001-9908-7860

**Yu-ya Ohnishi** − *JSR Corporation, Kawasaki, Kanagawa 210-0821, Japan*

**Takamitsu Matsubara** − *Graduate School of Science and Technology, Nara Institute of Science and Technology, Nara 630-0192, Japan; Data Science Center, Nara Institute of Science and Technology, Nara 630-0192, Japan*

**Tsuyoshi Ando** − *Graduate School of Science and Technology, Nara Institute of Science and Technology, Nara 630-0192, Japan;* orcid.org/0000-0001-5186-3867

**Tetsunori Sugawara** − *JSR Corporation, Yokkaichi, Mie 510-8552, Japan*

**Mikiya Fujii** − *Graduate School of Science and Technology, Nara Institute of Science and Technology, Nara 630-0192, Japan; Data Science Center, Nara Institute of Science and Technology, Nara 630-0192, Japan;* orcid.org/0000-0002-3728-3097

Complete contact information is available at: https://pubs.acs.org/10.1021/acsomega.6c06915


### Notes

This work was previously posted as a preprint on ChemRxiv (not peer reviewed): DOI: 10.26434/chemrxiv.10002084/v3
The authors declare no competing financial interest.

## ■ ACKNOWLEDGMENTS

This paper is based on the results obtained from a project, JPNP14004, subsidized by the New Energy and Industrial Technology Development Organization (NEDO).

## ■ REFERENCES


(1) Schweer, J. Penultimate Model Description of the Propagation Kinetics for the Free Radical Copolymerization of Styrene and Methyl Methacrylate. *Makromol. Chem., Theory Simul.* **1993**, *2* (3), 485−502.

(2) Willemse, R. X. E.; Van Herk, A. M. Copolymerization Kinetics of Methyl Methacrylate-Styrene Obtained by PLP-MALDI-ToF-MS. *J. Am. Chem. Soc.* **2006**, *128* (13), 4471−4480.

(3) Autzen, A. A. A.; Beuermann, S.; Drache, M.; Fellows, C. M.; Harrisson, S.; Van Herk, A. M.; Hutchinson, R. A.; Kajiwara, A.; Keddie, D. J.; Klumperman, B.; Russell, G. T. Experimental Methods and Data Evaluation Procedures for the Determination of Radical Copolymerization Reactivity Ratios from Composition Data (IUPAC Recommendations 2025). *Pure Appl. Chem.* **2025**, *97* (11), 1455−1463.

(4) Mayo, F. R.; Lewis, F. M. Copolymerization, I. A Basis for Comparing the Behavior of Monomers in Copolymerization; The Copolymerization of Styrene and Methyl Methacrylate. *J. Am. Chem. Soc.* **1944**, *66*, 1594−1601.

(5) Zapata-González, I.; Saldívar-Guerra, E.; Hutchinson, R. A. 80 Years of the Mayo Lewis Equation. A Comprehensive Review on the Numerical Estimation Techniques for the Reactivity Ratios in Typical and Emerging Copolymerizations. *Prog. Polym. Sci.* **2025**, *163*, 101956.

(6) Skeist, I. Copolymerization: The Composition Distribution Curve. *J. Am. Chem. Soc.* **1946**, *68* (9), 1781−1784.

(7) Fineman, M.; Ross, S. D. Linear Method for Determining Monomer Reactivity Ratios in Copolymerization. *J. Polym. Sci.* **1950**, *5* (2), 259−262.

(8) Kelen, T.; Tüdős, F. Analysis of the Linear Methods for Determining Copolymerization Reactivity Ratios. I. A New Improved Linear Graphic Method. *J. Macromol. Sci.-Chem.* **1975**, *9* (1), 1−27.

(9) Van Herk, A. M.; Dröge, T. Nonlinear Least Squares Fitting Applied to Copolymerization Modeling. *Macromol. Theory Simul.* **1997**, *6* (6), 1263−1276.

(10) Scott, A. J.; Penlidis, A. Computational Package for Copolymerization Reactivity Ratio Estimation: Improved Access to the Error-in-Variables-Model. *Processes* **2018**, *6* (1), 8.
(11) Behnken, D. W. Estimation of Copolymer Reactivity Ratios: An Example of Nonlinear Estimation. *J. Polym. Sci., Part A* **1964**, *2* (2), 645−668.
(12) Tidwell, P. W.; Mortimer, G. A. An Improved Method of Calculating Copolymerization Reactivity Ratios. *J. Polym. Sci., Part A* **1965**, *3* (1), 369−387.
(13) Fukuda, T.; Ma, Y.-D.; Inagaki, H. Free-Radical Copolymerization. 3. Determination of Rate of Propagation and Termination for the Styrene/Methyl Methacrylate System. A Critical Test of Terminal-Model Kinetics. *Macromolecules* **1985**, *18* (1), 17−26.
(14) Fukuda, T.; Kubo, K.; Ma, Y.-D.; Inagaki, H. Free-Radical Copolymerization V. Rate Constants of Propagation and Termination for a Styrene/ Methyl Methacrylate/Toluene System. *Polym. J.* **1987**, *19* (5), 523−530.
(15) Meyer, V. E. Reactivity Ratios of Styrene and Methyl Methacrylate at 90 °C. *J. Polym. Sci. A-1* **1967**, *5* (6), 1289−1296.
(16) Debnath, D.; Baughman, J. A.; Datta, S.; Weiss, R. A.; Pugh, C. Determination of the Radical Reactivity Ratios of 2-(N-Ethylperfluorooctanesulfonamido)Ethyl Acrylate and Methacrylate in Copolymerizations with N,N-Dimethylacrylamide by in Situ 1 H NMR Analysis As Established for Styrene−Methyl Methacrylate Copolymerizations. *Macromolecules* **2018**, *51*, 7951−7963.
(17) Ito, T.; Otsu, T. Solvent Effect in Radical Copolymerization of Methyl Methacrylate with Styrene. *J. Macromol. Sci., Pure Appl. Chem.* **1969**, *3* (2), 197−203.
(18) Zhang, H.; Hong, K.; Jablonsky, M.; Mays, J. W. Statistical Radical Copolymerization of Styrene and Methyl Methacrylate in a Room Temperature Ionic Liquid. *Chem. Commun.* **2003**, *3* (12), 1356−1357.
(19) Junkers, T. Precision Polymer Design in Microstructured Flow Reactors: Improved Control and First Upscale at Once. *Macromol. Chem. Phys.* **2017**, *218* (2), 1600421.
(20) Lauterbach, F.; Abetz, V. Continuous Kinetic Sampling of Flow Polymerizations via Inline UV−Vis Spectroscopy. *Macromol. Rapid Commun.* **2020**, *41* (9), 2000029.
(21) Reis, M. H.; Davidson, C. L. G.; Leibfarth, F. A. Continuous-Flow Chemistry for the Determination of Comonomer Reactivity Ratios. *Polym. Chem.* **2018**, *9* (13), 1728−1734.
(22) Brocken, L.; Price, P. D.; Whittaker, J.; Baxendale, I. R. Continuous Flow Synthesis of Poly(Acrylic Acid): Via Free Radical Polymerisation. *React. Chem. Eng.* **2017**, *2* (5), 662−668.
(23) Zhou, Y.; Han, S.; Gu, Y.; Chen, M. Facile Synthesis of Gradient Copolymers Enabled by Droplet-Flow Photo-Controlled Reversible Deactivation Radical Polymerization. *Sci. China Chem.* **2021**, *64* (5), 844−851.
(24) Achi, N. El.; Bakkour, Y.; Adhami, W.; Molina, J.; Penhoat, M.; Azaroual, N.; Chausset-Boissarie, L.; Rolando, C. Metal-Free ATRP Catalyzed by Visible Light in Continuous Flow. *Front. Chem.* **2020**, *8* (9), 740.
(25) Hornung, C. H.; Guerrero-Sanchez, C.; Brasholz, M.; Saubern, S.; Chiefari, J.; Moad, G.; Rizzardo, E.; Thang, S. H. Controlled RAFT Polymerization in a Continuous Flow Microreactor. *Org. Process Res. Dev.* **2011**, *15* (3), 593−601.
(26) Wakiuchi, A.; Takasuka, S.; Asano, S.; Hashizume, R.; Nag, A.; Hatanaka, M.; Miyao, T.; Ohnishi, Y.; Matsubara, T.; Ando, T.; Sugawara, T.; Fujii, M.; Ajiro, H. Composition Regulation by Flow Copolymerization of Methyl Methacrylate and Glycidyl Methacrylate with Free Radical Method. *Macromol. Mater. Eng.* **2023**, *308* (6), 2200626.
(27) Nag, A.; Wakiuchi, A.; Takasuka, S.; Asano, S.; Hashizume, R.; Hatanaka, M.; Miyao, T.; Ohnishi, Y.; Matsubara, T.; Ando, T.; Sugawara, T.; Fujii, M.; Ajiro, H. Investigation on Regulated Copolymer Composition in Free-Radical Flow Polymerization through Tube Length Variation. *MRS Commun.* **2025**, *15*, 1122.
(28) Takasuka, S.; Ito, S.; Oikawa, S.; Harashima, Y.; Takayama, T.; Nag, A.; Wakiuchi, A.; Ando, T.; Sugawara, T.; Hatanaka, M.; Miyao, T.; Matsubara, T.; Ohnishi, Y.-Y.; Ajiro, H.; Fujii, M. Bayesian Optimization of Radical Polymerization Reactions in a Flow Synthesis System. *Sci. Technol. Adv. Mater.:Methods* **2024**, *4* (1), 2425178.
(29) Yamada, H.; Takasuka, S.; Oikawa, S.; Harashima, Y.; Takayama, T.; Nag, A.; Wakiuchi, A.; Ando, T.; Sugawara, T.; Hatanaka, M.; Miyao, T.; Matsubara, T.; Ohnishi, Y.; Ajiro, H.; Fujii, M. Multi-Objective Bayesian Optimization for Experimental Design in Copolymerization and Revealing Chemical Mechanism of Pareto Fronts. *ACS Appl. Eng. Mater.* **2025**, *3*, 2402−2415.
(30) Haven, J. J.; Junkers, T. Online Monitoring of Polymerizations: Current Status. *Eur. J. Org. Chem.* **2017**, *2017* (44), 6474−6482.
(31) Al Azri, N.; Clifford, C.; Enick, R. M.; Veser, G. Impact of Flow Configurations on Response Time and Data Quality in Real-Time, In-Line Fourier Transform Infrared (FTIR) Monitoring of Viscous Flows. *Org. Process Res. Dev.* **2024**, *28* (5), 1657−1667.
(32) Schrecker, L.; Dickhaut, J.; Holtze, C.; Staehle, P.; Wieja, A.; Hellgardt, K.; Hii, K. K. M. An Efficient Multiparameter Method for the Collection of Chemical Reaction Data via 'One-Pot' Transient Flow. *React. Chem. Eng.* **2023**, *8* (12), 3196−3202.
(33) Pasquale, A. J.; Long, T. E. Real-Time Monitoring of the Stable Free Radical Polymerization of Styrene via in-Situ Mid-Infrared Spectroscopy. *Macromolecules* **1999**, *32* (23), 7954−7957.
(34) Smith, B. C. Infrared Spectroscopy of Polymers X: Polyacrylates. *Spectroscopy* **2023**, *38*, 10−14.
(35) Wakiuchi, A.; Jasial, S.; Asano, S.; Hashizume, R.; Hatanaka, M.; Ohnishi, Y. Y.; Matsubara, T.; Ajiro, H.; Sugawara, T.; Fujii, M.; Miyao, T. Multiple Comonomer Concentrations Prediction from FTIR Spectra with Quantum Chemistry-Based Interpretation. *MRS Commun.* **2024**, *14*, 439−444.
(36) Wakiuchi, A.; Jasial, S.; Asano, S.; Hashizume, R.; Hatanaka, M.; Ohnishi, Y. Y.; Matsubara, T.; Ajiro, H.; Sugawara, T.; Fujii, M.; Miyao, T. Chemometrics Approach Based on Wavelet Transforms for the Estimation of Monomer Concentrations from FTIR Spectra. *ACS Omega* **2023**, *8* (22), 19781−19788.
(37) Tibshirani, R. Regression Shrinkage and Selection via the Lasso. *J. R. Statist. Soc. B* **1996**, *58* (1), 267−288.
(38) Pedregosa, F.; Varoquaux, G.; Gramfort, A.; Michel, V.; Thirion, B.; Grisel, O.; Blondel, M.; Prettenhofer, P.; Weiss, R.; Dubourg, V.; Vanderplas, J.; Passos, A.; Cournapeau, D.; Brucher, M.; Perrot, M.; Duchesnay, E.ᵔ. Scikit-Learn: Machine Learning in Python. *J. Mach. Learn. Res.* **2011**, *12*, 2825−2830.